APPLIED GEOPHYSICS, Vol.10, No.2 (June 2013), P. 157-169, 14 Figures.
DOI: 10.1007/s11770-013-0374-4

Integrated application of 3D seismic and microseismic data in the development of tight gas reservoirs*

Yang Rui-Zhao[1], Zhao Zheng-Guang[1♦], Peng Wei-Jun[1], Gu Yu-Bo[1], Wang Zhan-Gang[1], and Zhuang Xi-Qin[2]

Abstract: The development of unconventional resources, such as shale gas and tight sand gas, requires the integration of multi-disciplinary knowledge to resolve many engineering problems in order to achieve economic production levels. The reservoir heterogeneity revealed by different data sets, such as 3D seismic and microseismic data, can more fully reflect the reservoir properties and is helpful to optimize the drilling and completion programs. First, we predict the local stress direction and open or close status of the natural fractures in tight sand reservoirs based on seismic curvature, an attribute that reveals reservoir heterogeneity and geomechanical properties. Meanwhile, the reservoir fracture network is predicted using an ant-tracking cube and the potential fracture barriers which can affect hydraulic fracture propagation are predicted by integrating the seismic curvature attribute and ant-tracking cube. Second, we use this information, derived from 3D seismic data, to assist in designing the fracture program and adjusting stimulation parameters. Finally, we interpret the reason why sand plugs will occur during the stimulation process by the integration of 3D seismic interpretation and microseismic imaging results, which further explain the hydraulic fracture propagation controlling factors and open or closed state of natural fractures in tight sand reservoirs.

Keywords: tight sand gas, 3D seismic, microseismic, reservoir characterization, hydraulic fracture, and fracture barrier

Introduction

Unconventional tight gas engineering factors play a predominant role in the early stages of unconventional tight gas development. The low (sub-millidarcy) permeability reservoirs require multiple engineering disciplines to develop solutions for extended laterals with multi-stage hydraulic fracture stimulation completion strategies to achieve economic production levels (Rutledge and Phillips, 2003). The completion objective is to maximize reservoir contact through the generation of fracture networks to increase the permeability and allow for the movement of gas through the reservoir and into the production well (Frohne and Mercer, 1984).

Microseismic monitoring provides the means to characterize the induced fracture networks generated by hydraulic fracture stimulation and determine the stimulated reservoir extent to optimize drainage (Grechka et al., 2010). The fluids injected during hydraulic fracture stimulation will change the reservoir stress field, which results in the failure of the rock and the release of energy due to fracturing. The released energy propagates in the form of seismic waves called "microseismic waves"

Manuscript received by the Editor October 17, 2012 ; revised manuscript received April 17, 2013.
1. School of Geoscience and Surveying Engineering, China University of Mining & Technology, Beijing 100083, China.
2. Geophysical Prospecting Company of SINOPEC North China Bureau, Xinxiang 453000, China.
♦Corresponding Author: Zhao Zheng-Guang (Email: robin_chiu@foxmail.com)

due to their ultralow magnitude (below 0 magnitude) (Maxwell, 2010; Shemeta and Anderson, 2010) and can be recorded by surface geophones. The recorded microseismic data can be processed to determine the magnitude and location associated with the fracture.

Microseismic monitoring of hydraulic fractures has become the conventional procedure in the completion of unconventional tight gas wells. Evaluating fracturing results by use of microseismic imaging is common in all tight gas fields in the world. Through the processing and interpretation of microseismic data, accurate fracture orientation, geometry, and dimensions, as well as an image of fluid flow passage in the induced fracture network can be determined. In addition, microseismic monitoring can provide images of the hydraulic fractures that change with time, thus providing non-substitutable information for theoretical research and technological development of the hydraulic fracture method (Song et al., 2008).

3D seismic data can be used in reservoir characterization to better understand reservoir heterogeneity. Seismically derived properties, such as the curvature attribute, ant-tracking cube, and relative acoustic impedance, can be used to study reservoir fracture distribution and the horizontal stress direction in order to get reservoir geomechanical property-related information to guide hydraulic fracture stimulation (Hart, 2006). In addition, the characterization of small faults and fractures by 3D seismic data can determine the local horizontal stress direction and identify potential barriers that could affect hydraulic fracture propagation as well as assist in interpreting microseismic data (Refunjol et al., 2011, 2012). In this study, we integrate various geophysical methods in mapping reservoir heterogeneity and validate the results by microseismic monitoring data.

Geological setting

Regional overview

Daniudi Gas Field is located in the border region of Yulin City, Shaanxi, and Ordos City, Inner Mongolia, which is structurally located in the east section of the northern part of the Yishan Ramp of the Ordos Basin and has an area of more than 2 000 km2. Sulige Gas Field is located to the SW-SWW direction of Daniudi Gas Field and the Wushenqi and Jingbian Gas Fields to the SW direction. Yulin and Zizhou Gas Fields are to the south and Mizhi Gas Field is to the SSE (Duan et al., 2009).

In Daniudi Gas Field, faults are not developed but there are some nose-like uplifts in the local area. The overall structure is one gentle monocline with an average slope of 6 to 9 m/km, where the NE part is higher and the SW part is lower. From the bottom up, the Daniudi Gas Field strata are divided into Ordovician, Carboniferous, Permian, Triassic, Jurassic, Cretaceous, and Quaternary systems. Permian strata are divided into the Shanxi, Lower Shihezi, Upper Shihezi, and Shiqianfeng formations. The Lower Shihezi Formation, which mainly consists of a tight, low permeability, sandstone gas reservoir, is the major exploration and development target (Lin et al., 2011).

Reservoir overview

The stimulation target is the He1 Member tight sandstone layer of the Lower Permian Series Lower Shihezi Formation, which has a vertical depth of 2534 m and is mainly composed of quartz debris sandstone. Quartz content of the clastic particles is 56 to 84% with an average value of 73.3%, feldspar content is 0 to 7% with average value 2.4%, and debris content is 16 to 37% with average value 24.3%. The rock is grain-supported and pore-cemented and the grains contact with each other in point-line form. The argillaceous matrix content of the He1 Member reservoir is 0 to 15 % with average value 4.1%. The authigenetic cements include quartz, kaolinite, chlorite, illite, calcite, and dolomite. The He1 Member reservoir has low porosity and permeability. The average reservoir porosity is 10.31% and the average permeability is 0.76 mD. The He1 Member reservoir porosity is distributed between 8% and 14% and has a distribution frequency of 82.14%. The reservoir permeability distribution is between 0.25 and 2.0 mD with the proportion of permeability larger than 0.25 mD is 85.71%.

The prediction from 3D seismic data shows that the horizontal laterals of the DP43 horizontal well group is located in the favorable areas for quartz sandstone, where the quartz sandstone thickness is greater than 24 m and its effective thickness is greater than 6 m. Taking Well B as an example, the mud log shows that the total horizontal length of this well is 946.04 m and the total drilled sandstone length is 921.21 m, which is 97.38% of the total horizontal length. The total sandstone length with hydrocarbon shows is 350 m, which is 37% of the total horizontal length. The total drilled mudstone and siltstone length is 24.83 m, which is 2.62% of the total horizontal length. The seismic inverted porosity shows that the horizontal section of Well B is located in the zone of relative higher porosity which is indicated by the red and yellow colors in Figure 1.

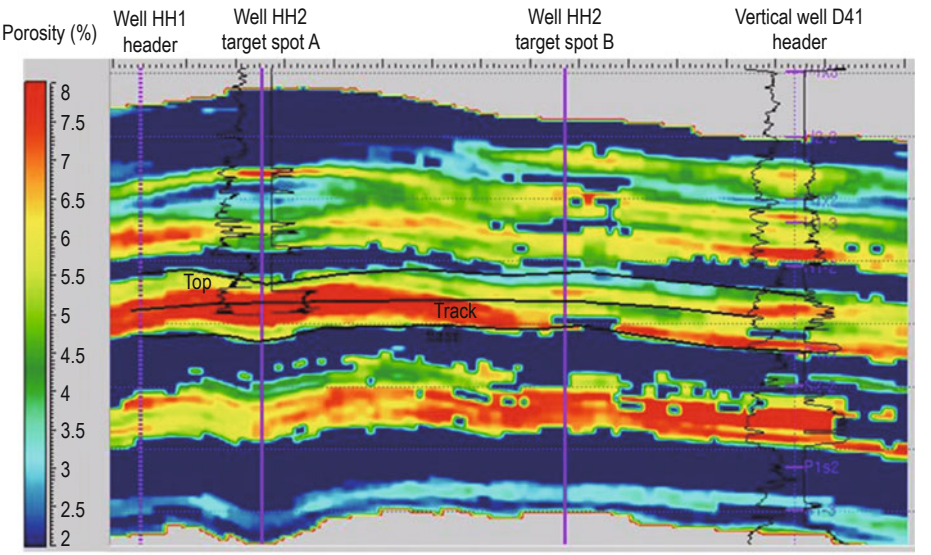

Fig.1 Seismic derived porosity profile showing the horizontal section of Well HH2.
The three solid lines represent the interpreted seismic horizon of the reservoir top, the horizontal section of Well HH2, and the interpreted seismic horizon of the reservoir bottom, respectively

Well group overview

As shown in Figure 2, the cluster horizontal well group, consisting of wells HH1, HH2, HH3, HH4, HH5, and HH6, is located in Erlintu Town, Shenmu County, Yulin City of Shaanxi Province. The well group is structurally located in the northeast part of the Yishan Slope in the Ordos Basin. The target strata of the six wells are the Lower Permian He1 Member of the Lower Shihezi Formation. All of the horizontal sections of the six wells are about 1000 m in length. The end point of each horizontal well is target spot B, indicated by B in Figure 2 and the completion method is open-hole completion. The area of the well site is 204 x 120 m, the distances between two well heads in the same row are 67 and 69 m and the distances in the same array are 4.2, 4.4, and 4.3 m.

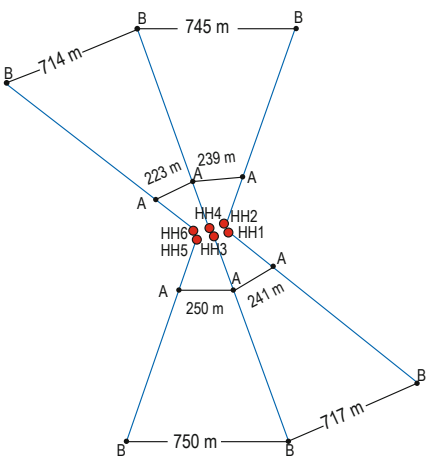

Fig.2 Layout of the cluster six-horizontal well group.

A and B are the target spots A and B of each well. The red dots are the projections of the six well heads. The distances noted on the figure are the distances between the two target spots A or two target spots B of adjacent horizontal wells.

3D Seismic method

Determining the local stress direction using the curvature attribute

To determine the fault or fracture orientation and horizontal stress direction, the rose diagram derived from image logs is a direct and effective way. However, when there are no image logs, the curvature attribute extracted from 3D post-stack seismic data is one indirect approach (Blumentritt et al., 2006; Chopra and Marfurt, 2007a, 2008).

Curvature attributes measure the structural shape of the seismic data, among which the most positive curvature can highlight anticlinal features, especially hinge zones. Nelson (2001) describes how zones of greatest curvature relate to the zones of greatest strain in the rock. The relation between curvature and strain allows us to use curvature measured from 3D seismic to infer fractures.

One alternative method to determine fault or fracture orientation is interpreting the lineament features of faults or fractures on a horizon-based curvature map derived

from 3D seismic data and then transform them into a rose diagram which is similar to that obtained from image logs (Chopra and Marfurt, 2007b, 2010).

Figure 3 shows the most positive curvature distribution in the range which is composed by target spot B of each horizontal well of the six-well group. The azimuthal rose diagram embedded in the upper right of Figure 3 is generated by interpreting the curvature attribute (curvature distribution map). It shows that the direction of the present-day maximum horizontal principal stress is about 85°, perpendicular to which is the direction of present-day minimum horizontal principal stress.

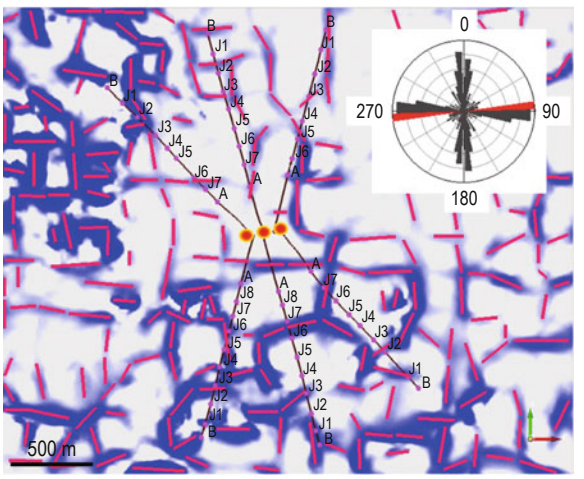

Fig.3 Curvature attribute predicts the direction of maximum horizontal principal stress.

The embedded diagram in the upper right is the azimuthal rose diagram which shows the direction of the present-day maximum horizontal principal stress is about 85°.

Determining whether the natural fractures are open or closed using curvature attributes

Although curvature can measure relative bending and structural deformation and possible fractures at the time of deformation, we need to estimate the present day stress field from borehole breakouts, image logs, and azimuthal anisotropy measurements. From the borehole breakouts of the six wells, the present day local stress of the well group (smallest rectangular area containing the target B points of each well) is estimated along the NE85° (see the inset diagram in Figure 4) so that the fractures aligned in this direction will be open and the perpendicular fractures will be closed (Yenugu and Marfurt, 2011).

Figure 4 shows the most positive principal curvature horizon slice of the six-well group target reservoir with the fractures hypothesized on the hinge zones indicated by red color. The fractures aligning with the present day stress should be open (indicated by blue arrows) and the fractures aligned perpendicular to the present day stress should be closed (shown by black arrows). The horizontal sections which are drilled through open fractures are expected to be prone to fractures. However, the horizontal sections which are surrounded by closed fractures will be difficult to fracture, or worse, sand plugs will occur since the closed fractures obstruct hydraulic fracture propagation.

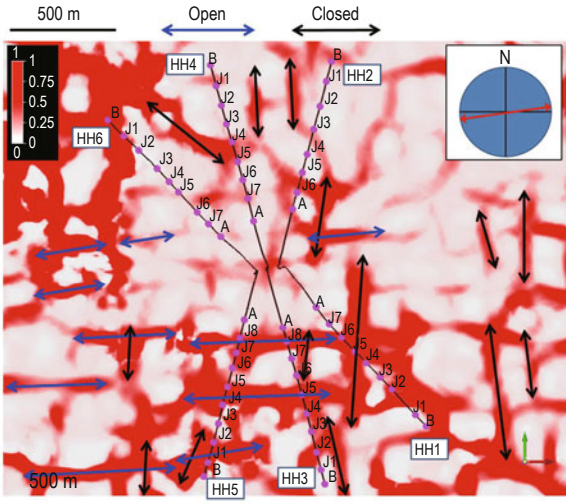

Fig.4 The curvature attribute integrated with borehole breakouts determining whether the natural fractures are open or closed.

The blue and black arrows represent the identification of open and closed fracture zones inferred from present day stress information. The direction of the present day stress measured from borehole breakouts is shown in red in the upper-right inset diagram.

Fault mapping using the ant-tracking volume

Understanding the fault geometry is essential in the characterization of the reservoir. The presence of faults can pose drilling hazards as well as influence the completion of the well. Locally varying stress fields deviating from the regional stress directions can result due to the presence of faults and influence fracture propagation. In this study, we have tracked and detected those small faults around the target reservoir of the six-well group within the 3D seismic volume using the ant-tracking technique. Then we extracted the distribution map of small faults which is ready to be integrated with the curvature distribution map for further study.

The ant-tracking algorithm was utilized to generate a fault volume. Several steps are involved in the workflow including data pre-condition, edge detection, and ant-tracking. The data pre-conditioning step applies an edge preserving smoother to the input seismic data in order to enhance reflection event continuity while preserving

discontinuous events corresponding to the presence of faults. Next, an edge detection method is implemented to extract features that represent discontinuities in the seismic image. This process, however, will detect all discontinuities including faults, channel boundaries, acquisition footprint, reflection amplitude variations, and various other features that disrupt reflector continuity. The ant-tracking algorithm then extracts features within the edge detection volume that exhibit fault-like behavior. It uses principles from ant colony systems to extract like trends in a noisy data environment. This algorithm emulates the behavior of ant colonies in nature and how they use pheromones to mark their paths in order to optimize the search for food. It reaches the optimum result mainly by the information delivery in the so called "artificial ant" intelligent swarm, which makes ants prone to choose the path that has higher pheromones concentration and finally reach the optimum path by updating information continuously (Shi, 2009; Zhang, 2010).

Digital intelligent agents (ants) are distributed throughout the edge detection volume and extract features that exhibit characteristics consistent in dip, azimuth, planarity, and spatial continuity. The output is then an attribute volume that corresponds to only fault-like features. The ant-tracking results were used to identify existing faults and provide an indication of areas with stress variations. The stress variations manifest in the form of velocity changes that can be detected by seismic amplitude measurements. Therefore, discontinuities in the seismic image that do not exhibit an observable reflector displacement can indicate areas of increased stress (subseismic resolution faults that are likely to be still tectonically located) where these areas would be prone to strain release upon an increase in effective stress as a result of the hydraulic fracture treatment (Nortan et al., 2011; Maxwell et al., 2011).

Integration of curvature and ant-tracking volumes to predict potential fracture barriers

When the orientation of local faults or fractures is identical to the direction of regional horizontal principal stress, the faults or fractures are generally open or filled by shale. In this case, the reservoir formation would be easy to fracture under hydraulic pressure or fracturing fluids leakage would even occur, for these conductive faults or fractures provide the fracturing fluids with flow paths. However, when the direction of local small faults or fractures is perpendicular to or oblique crossing at high angle with the direction of the regional horizontal principal stress, in which case the faults or fractures would be closed, then during the hydraulic fracture stimulation, these faults could form fracture barriers where the energy can be dissipated along existing faults and the hydraulic fractures would stop propagating. In some extreme circumstances, sand plugs will occur (Ringrose et al., 2009). As a consequence, predicting potential fracture barriers before executing well stimulation is necessary for optimizing well stimulation design and avoiding sand plugs.

In this study, we have first determined the orientation and open or close state of the faults or fractures and then identified the potential fracture barriers in the ant-tracking result map. As shown in Figure 5, the F1, F2, F3, F4, F5, F6, F7, and F8 faults are predicted to be closed and will probably act as fracture barriers.

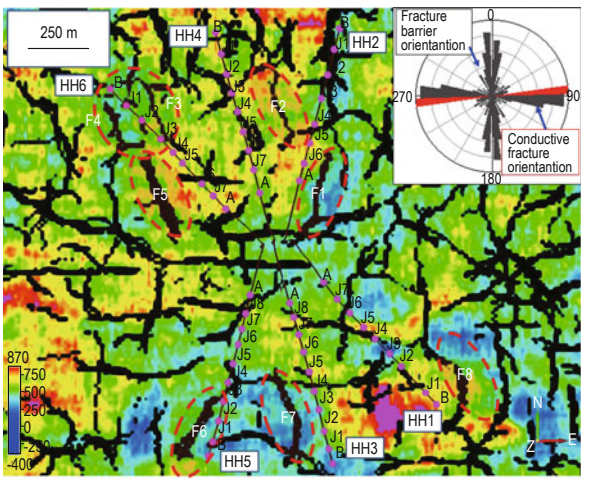

Fig.5 Horizon slice of ant-tracking volume predicting potential fracture barriers.

The small faults in the shadowed ellipses are predicted to be potential fracture barriers. The fracture strikes are identical to the fracture barrier orientation while perpendicular to the conductive fracture orientation shown in the upper-right inset diagram.

Microseismic monitoring

Stimulation program

In the case of simultaneously fracturing two adjacent wells, the hydraulic fracture propagation space of one well will constrain the hydraulic fracture propagation space of the other well. The net pressure within the fractures will increase, which makes the hydraulic fractures more complex and the stimulated reservoir volume much larger. However, because the horizontal sections of the two adjacent wells, especially the two

fracturing stages near the target spot A will be less than 250 m apart (as shown in Figure 1) and the reservoir will be easily penetrated and consequently the simultaneous fracturing will fail if inappropriate stimulation parameters are chosen. To avoid this situation, only two adjacent wells with potential fracture barriers in between should be chosen for simultaneous fracturing based on the fault and fracture interpretation from the 3D seismic curvature and ant-tracking volumes. For wells HH1, HH3, and HH5, a relatively higher density of open fractures exist between the horizontal sections of wells HH1 and HH3 and the two hydraulic fracture sets are expected to easily communicate with each other. Potential fracture barriers exist between wells HH3 and HH5, indicating that simultaneously fracturing wells HH3 and HH5 is a better choice with lower failure risk. Using the same analysis, simultaneously fracturing wells HH4 and HH6 is determined because potential fracture barriers and closed fractures exist between them. Based on this analysis, the stimulation program of the six-well group is finally determined that well HH2 (seven stages) will be fractured first, well HH1 (seven stages) will be fractured second, wells HH4 (eight stages) and HH6 (eight stages) will be simultaneously fractured, and finally, wells HH3 (nine stages) and HH5 (nine stages) will be simultaneously fractured.

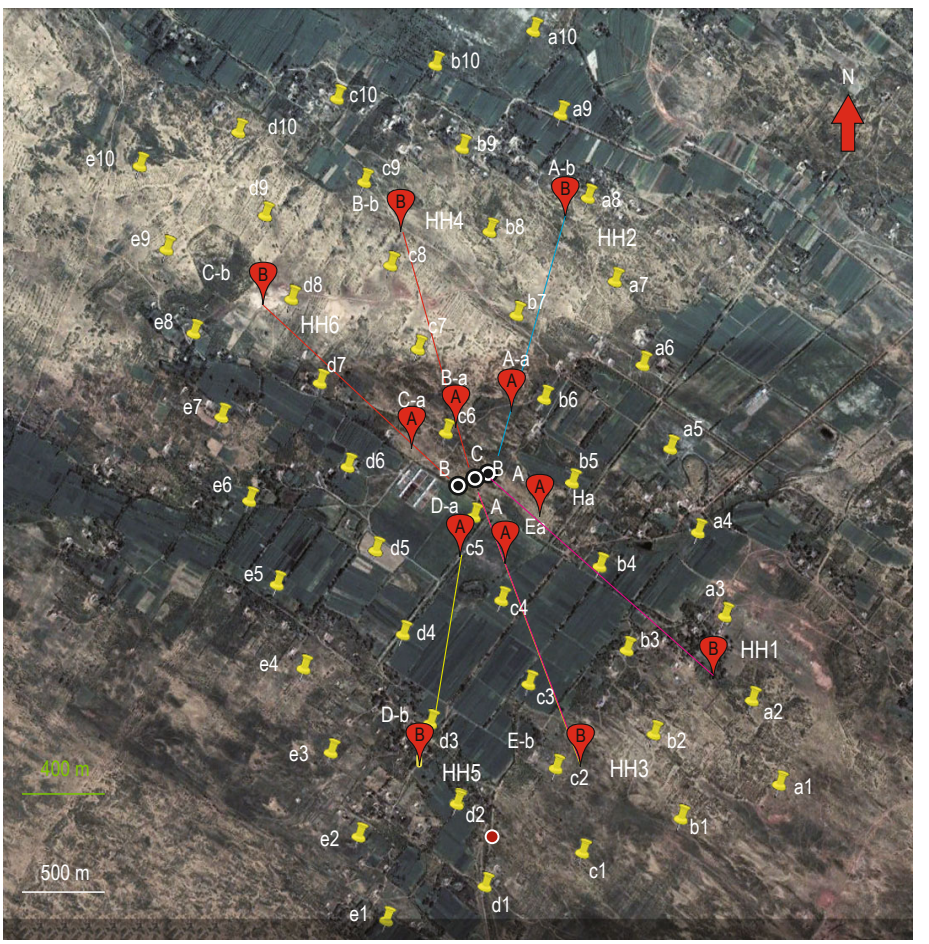

Fig.6 Layout of the microseismic monitoring surface geophone array.
The yellow pins are surface geophone locations. The solid lines of different colors represent the horizontal section projections of different wells. The wells with the same color will be fractured simultaneously.

Data acquisition

During hydraulic fracture stimulation treatment, the surface-based real-time microseismic monitoring is able to process the microseismic signals recorded by the surface digital geophones in real time. The live processing and interpretation of microseismic event locations allow the field engineers to assess and modify well stimulation designs and make appropriate changes to achieve better stimulation results while the stimulation treatment is in progress.

For the surface-based microseismic monitoring of the hydraulic fracturing of the six wells, the surface geophone array, which is a regular sparse grid centered on the six well heads, consists of 50 three-component (3-C) digital geophones buried 4 m below the ground surface which can reduce or even remove the noise from wind, vegetation cover, traffic, rig, rain drops, and etc. As shown in Figure 6, the 50 geophones are deployed in five lines which have an identical orientation of NW 20 °. The line interval is 500 m and the geophone interval on the same line is 400 m, which forms a grid having an area of 3600 m (Inline) × 2000 m (X-line). The Inline length of 3.6 km is 1.5 times the depth to the target stimulation reservoir, which satisfies the requirements for full-azimuth observation of each fracturing stage.

The buried geophones are 3-C digital geophones with a bandwidth of 0 to 800 Hz. The sensitivities of the vertical and horizontal components are 400 MV/CM/S ± 7.5 % and 400 MV/CM/S ± 10 %, respectively. The X horizontal components of all the geophones are oriented to the east. The microseismic signals are recorded at a 1 ms sampling rate and transferred to the central processing unit through wirelines for real-time processing. The geophones are initiated about 30 minutes before the stimulation begins in order to provide the background noise level for data processing method optimization.

One microseismic event will incur an amplitude increasing or spike on all the traces of all the geophones while random noises can only impact one or some of the geophones. Figure 7 shows the typical recorded seismic traces during the simultaneous stimulation, from which we can see that the S/N ratio is rather low and filtering is needed and to remove some obvious noise for event location. However, the spikes, which are just 2 seconds above the red line and appear in all of the traces of all the geophones, demonstrate that one microseismic event of a relatively large magnitude not commonly seen during fracturing has occurred at 3457 s since the station has begun to record data.

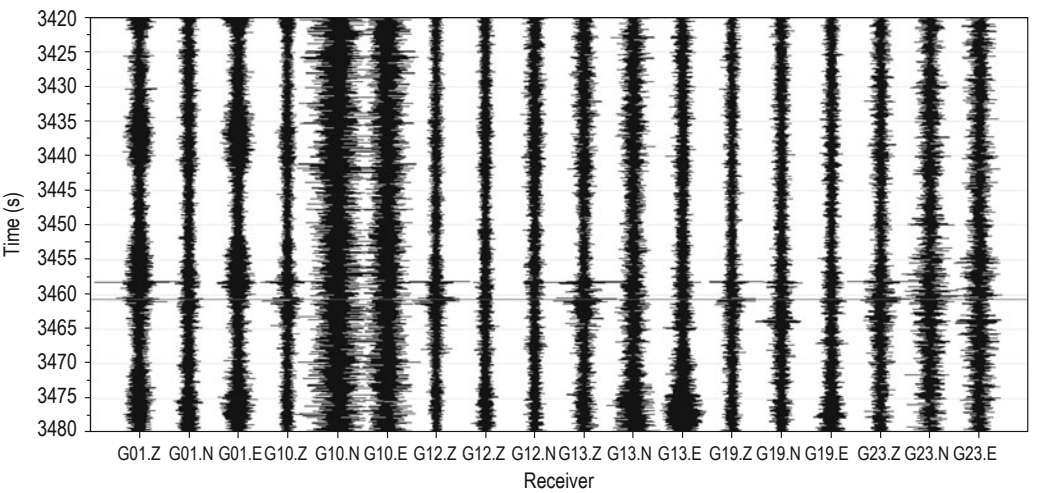

Fig.7 Typical recording showing one microseismic event of relatively large magnitude.
At two seconds above the red line, one microseismic event of relatively large magnitude not commonly seen during fracturing has occurred at 3457s since the station began recording data.

Data processing

First, the recorded seismic traces of three components of each geophone should be checked. If there are empty or damaged traces or the noise level is too high, the traces should be removed directly. The remaining effective data will be further processed to remove obvious noise and then be 1 to 45 Hz bandpass filtered. The high-cut frequency set to 45 Hz is mainly to remove the 50 Hz fixed frequency noise yielded by the generator in the well site.

The primary challenge of data processing is the separation of wavefield components that contain information about the microseismic signals from surface-generated noises, especially anthropogenic noises (Hanssen and Bussat, 2008). The surface-generated noise sources includes car and truck traffic, drilling operations, well fracture stimulations, pipelines, gas compressors, well production equipment, and wind in the survey area (Birkelo, et al, 2011). These noises can generally be categorized as the following two types based on their frequency bandwidth:

(1) Broadband transient noises, created by traffic, fauna, explosions, or falling objects; and (2) Narrow

bandwidth stationary sources created by machinery, running water, or the structural resonances of buildings or bridges (Vaidya, 2009).

Figure 8 shows the amplitude-frequency analysis result of the typical traces from an individual 3-C geophone which indicates that the microseismic traces recorded by the surface geophones have a frequency bandwidth of 1 to 75 Hz.

The noise from vehicles is typical broadband transient noise. Figure 9 shows the 3-C traces recorded by the geophone when a truck went near it. The surface tremors generated by the truck mainly propagate in the form of surface waves, so the two horizontal components, i.e. X component and Y component, have similar waveforms.

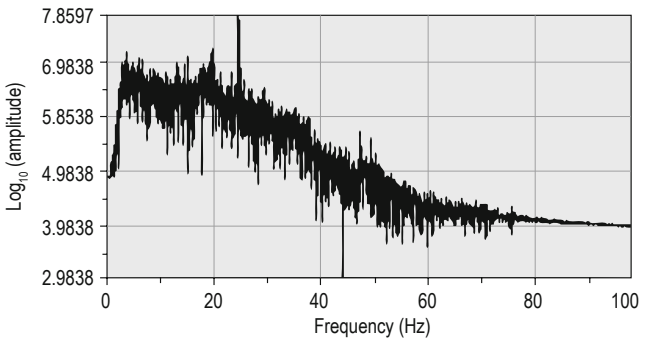

Fig.8 Amplitude-frequency spectrum of the 3-C traces of a single geophone.

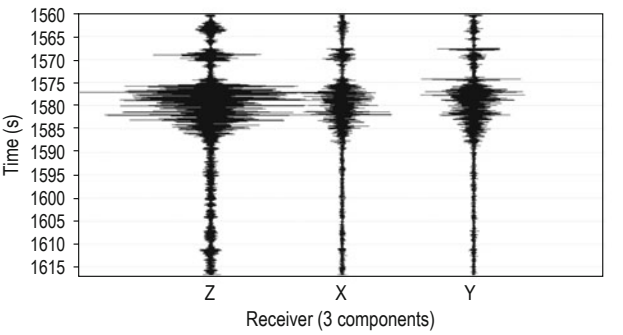

Fig.9 Waveforms of noise caused by a vehicle.

The wave amplitude of the vertical component, which is labeled Z in the figure, is much higher than that of the two horizontal components. This is because the vertical tremor generated by the truck is larger than the horizontal tremor. In addition, as the truck comes from far away to nearby, the tremors will endure a process of weak to strong and back to weak amplitude, which makes the seismic wave amplitude have the feature of low to high and then lower again. This amplitude feature is similar to the Doppler effect and the waveforms are like a spindle which can be easily identified in the original recordings.

Compared to the noise from a vehicle, the noise from human walking or object dropping is typical stationary noise sources with narrow bandwidth. The seismic traces in the red rectangle in Figure 10 show the tremors generated by a human walking. The individual spike pulse indicates that the human walking signal has a fixed frequency.

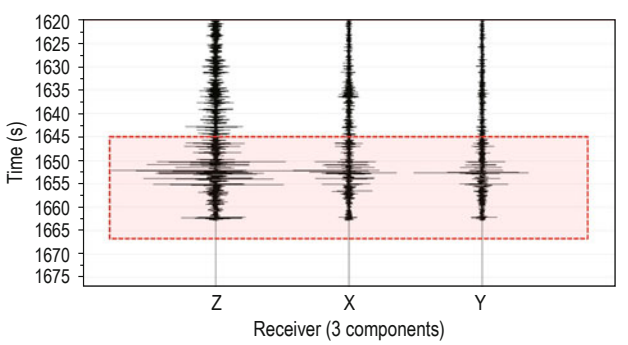

Fig.10 Waveforms of noise from human walking.

Since the traffic, pumping, generator, and engineers walking on the well site provide strong noise sources, the signals recorded by the geophones close to the well heads will be severely contaminated and the recorded microseismic data is not appropriate for event location. When recording the string shot signals by a star-shaped geophone array to correlate the velocity model, we also record the well site noises. Figure 11 shows the recorded seismic traces on one line. The line is 5 km long and consists of 200 vertical component geophones. The geophone that records the central trace is located in the center of the well site. From the figure, we see that the noises from the well site propagate in typical surface waveforms and attenuate quickly to the two sides and even dissipate at the distance of 1 km to the well site. From this analysis, we conclude that to avoid the well site noise, the geophones should be deployed beyond about 1 km to the well site, which ensures not only receiving effective signals but also avoiding much noise.

The noises from the well site are identified within the dashed ellipse and they propagate as typical surface waveforms and attenuate quickly to dissipate at the distance of 1 km to the well site.

Microseismic event location

Based on the time and wave field inversion process, microseismic inversion methods can be classified into travel-time and energy inversion.

Time difference of P-P or S-S wave methods and time difference of P and S wave methods are the two basic

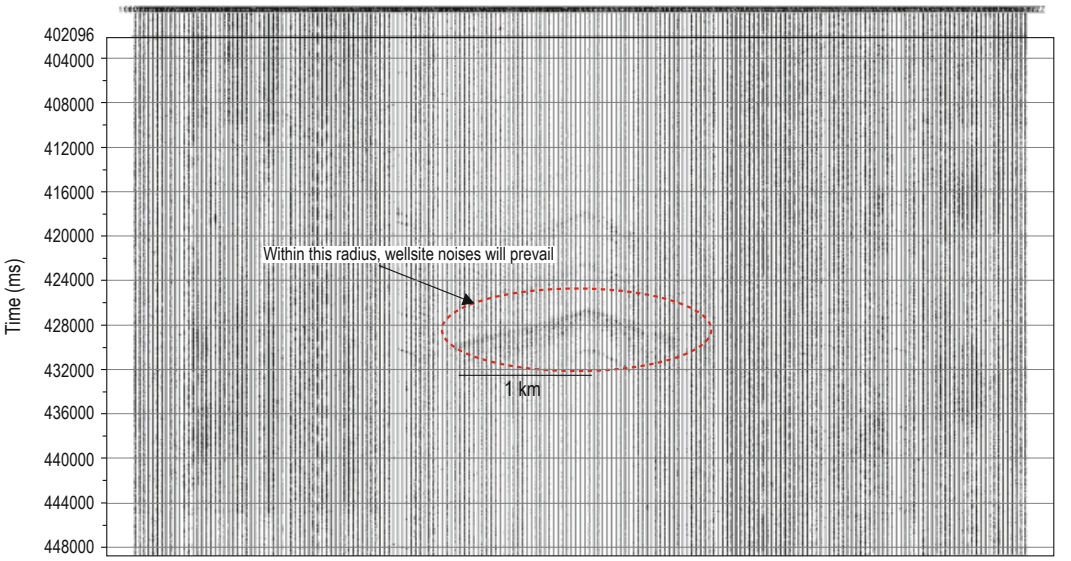

Fig.11 Seismic profile from one individual line of a star-shaped array.

methods for travel-time inversion. The methods can be further classified into vector diagram techniques based upon the particle motion of direct arrivals and triangulation schemes based upon arrival times of direct waves concerning the data processing approaches (Maxwell et al., 2010; Duncan and Eisner, 2010). These two classes require picking the P- and/or S-waves arrivals accurately. Since the microseismic data recorded by surface geophones usually have low signal-to-noise ratio and the arrivals cannot be identified in the original records, we have chosen the energy inversion method which does not need picking the arrival-times of P- or S-waves. The energy inversion algorithm is also called Seismic Emission Tomography which distinguishes the distribution of signal energy from both rock fracturing and background noises. The key procedure of the energy inversion algorithm is semblance stacking. The most widely used semblance stacking equation (Sheriff, 1991) is:

$$S(k) = \frac{\sum_{j=1}^{N}(\sum_{i=1}^{M} f_{ij})^2}{F},$$

where $S(k)$ is the coefficient of semblance which measures the correlation of point k in a time window having N samples in the vertical component traces in the array which has M geophones of artificial exploration survey, f ij is the record of the jth sample in ith trace i, i = 1, 2, … with M and j = 1, 2, …, N, and F is the appropriate normalization factor.

By stacking effective signals, the background noise will weaken, the fracturing energy will be enhanced, and the output will be the energy distribution map where the high amplitude fracturing energy is distributed on the low amplitude background noise energy (Kiselevitch et al., 1991; Lakings et al., 2006; Shen et al., 2009).

At first, single-dimensional P-wave and S-wave velocity models, which were created using available dipole sonic logs, are interpolated into 3D grids to establish velocity models. In most cases, there are no sonic logs which measure the shallow formations from surface to the low velocity zone and loess formation. Accurate velocity models for the shallow zone should be determined by analyzing the velocities of the drilled loess formation and surfaces of different lithologies. Typical velocities of different surface lithologies are listed in Table 1.

Table 1 Velocities of surfaces of different lithologies

Surface types	Velocity (km/s)
Desert	0.35 ~ 0.75
Loess tableland	0.5 ~1.2
Gobi Desert	0.5 ~1.0
Loess (Plain)	1.0 ~ 1.2
Wet sand (Phreatic Aquifer)	>1.5
Aquifer	1.4 ~ 1.5

After creating 3D velocity models, the travel-time difference (i.e., moveout across the array) table will be calculated based on the established velocity models. The times that the micro-fracturing signals emitted from certain areas surrounding the stimulated reservoir formation need to travel through the overlying formations to the surface buried geophones are different from each other, i.e., there is moveout when the signal travels across

the array. These travel-time differences are stored in the travel-time difference table. The 3D velocity model is divided into many grid nodes with a dimension of 20 m *20 m *20 m and the travel-time differences of the signals emitted from each grid space surrounding the stimulated reservoir formation are calculated and stored to create the theoretical travel-time difference table.

Then the squared difference sums of deviations from the theoretical travel-time differences to actual travel-time differences are calculated and recorded. The least sums of squared differences will be sought and the P- or S-waves first arrival amplitude responses which have reached the requirement of least sums of squared difference will be shifted based on the travel-time differences and then stacked. The stacked waveforms are finally expressed in seismic amplitude quadratics, defined as "energy". The position in 3D space of the energy emitted from the subsurface which satisfies the condition of least sum of squared difference is the microseismic event location.

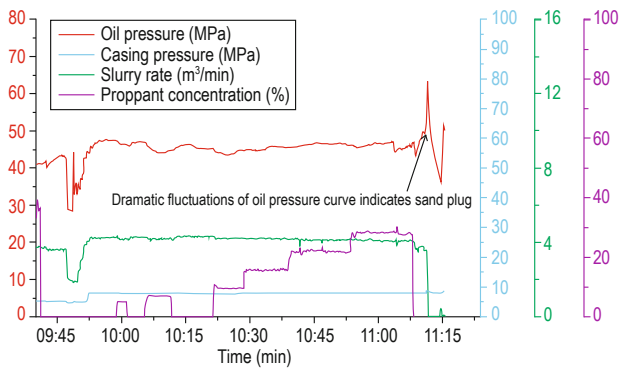

Fig.12 Parameter curves of the second stage stimulation of Well HH6.

Results and analyses

During the simultaneous stimulation of wells HH4 and HH6, sand plugging occurred at the second stage of well HH6 and the pumping pressure curves fluctuated wildly (See Figure 12). At that point, while the designed total input sand volume is 44.1 m^3, a sand volume of 37.8 m^3 has entered the reservoir formation during the stimulation which indicates that the hydraulic fractures have propagated to a certain distance and are blocked and no extra sand volume can be allowed to enter into the reservoir formation. Figure 13 shows the microseismic monitoring result of the second-stage simultaneous stimulation of wells HH4 and HH6. The space-temporal interpretation (as shown by red and blue solid lines, where red lines represent major fractures and blue lines indicate minor fractures) of the hydraulic fractures indicates that: (1) the orientation of the major hydraulic fractures of both wells is about NE85°. The hydraulic fracture propagation direction is identical and is controlled by the local maximum horizontal principle stress. (2) The left wing of the fractured zone of well HH6 has a length of 126.7 m and the right wing is 108.9 m. The left wing of the fractured zone of well HH4 has a length of 140.2 m and the right wing is 141.0 m. The fracture propagation length of well HH6 is obviously shorter than that of well HH4. Comparing with the fracture barriers predicted by 3D seismic data, this microseismic monitoring result proves that faults F3 and F4 are real fracture barriers. When the hydraulic fractures propagated from the wellbore along the direction of maximum horizontal principle stress (NE85°) to faults F3 and F4, the propagation distance, which is about 120 m, is relatively long and the fracturing energy dissipated along the faults and the hydraulic fractures stopped propagating at these fault locations.

Integrating the sand plug which occurred during the simultaneous stimulation of wells HH6 and HH4 with the microseismic monitoring results, the key parameters, i.e., slurry rate and proppant concentration for the simultaneous stimulation of wells HH3 and HH5 are modified to avoid another sand plug resulting from the existing fracture barriers. The curvature attribute and ant-tracking volume derived from 3D seismic data show that fracture barriers exist close to the first stage to the fifth stage, which indicates that the slurry rate and proppant concentration should be decreased to prevent the hydraulic fractures from propagating to the fracture barriers which would otherwise result in another sand plug. Taking the stimulation of the fourth stages of wells HH4 and HH5 as an example, the slurry rate and proppant concentration of well HH4 are 4.3 to 4.5 m^3/min and 46.8 m^3, respectively, while the slurry rate and proppant concentration of well HH5 is decreased to 4.2-4.3 m^3/min and 43.3 m^3 and the simultaneous stimulation has been normally implemented.

Owing to that the stimulation parameters have been promptly adjusted based on the results both of 3D seismic and microseismic data during the fracturing process, potential sand plugs have been successfully avoided. Among the 48 total stages of the six-well group, no sand plugs occurred during the stimulation of all the stages other than the second stage of well HH6. The reason why the sand plug occurred is that F3 and F4 faults, which appear in pairs, exist on each side of the second stage of well HH6, resulting in that the hydraulic

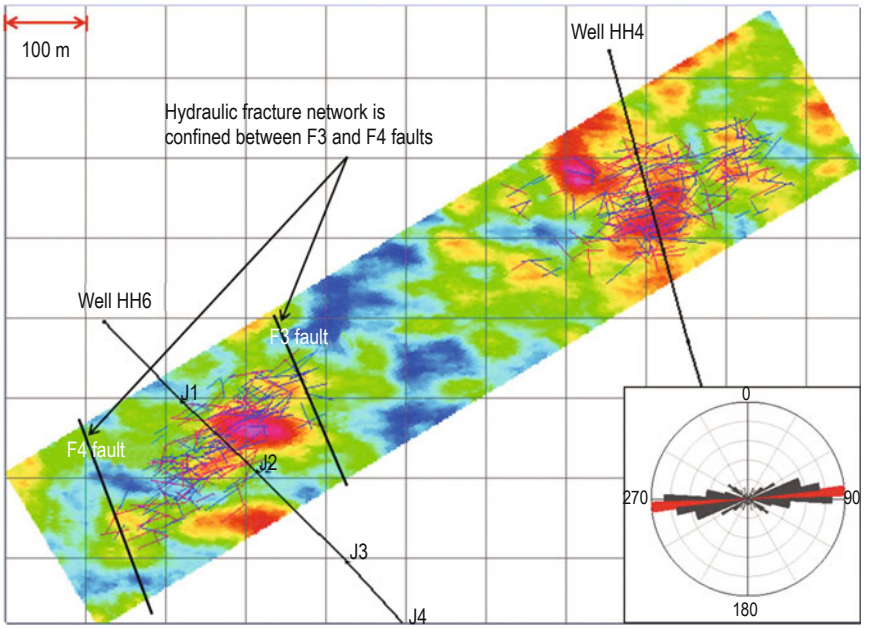

Fig.13 Microseismic monitoring results of the second stage stimulation of wells HH6 and HH4.
The distribution of energy is plotted as colored pixels, with higher energy values corresponding to warmer colors. The values of the color bar are in arbitrary units. The spatio-temporal interpretation is shown by red and blue solid lines, where red lines represent major fractures and blue lines stand for minor fractures. The embedded rose diagram in the lower right shows that the orientation of the major hydraulic fractures of both wells HH6 and HH4 is about NE85°.

fractures could not propagate farther, leading to the sand plug. However, the small closed faults, including F1, F2, F5, F6, F7, and F8, appear individually on one side of the fracturing stages. When the hydraulic fractures of one side of the stage could not propagate farther, the hydraulic fractures of the other side could propagate to a longer distance, resulting in no sand plugs. Taking the stimulation of the first and second stages of well HH1 as an example (see Figure 14a), the closed small faults of F8 near the fracturing stages has acted as a fracture barrier and prevented the hydraulic fractures from propagating in the NE direction, which led to the hydraulic fractures in the right wing of the first and second stages have a length of only 105.1 m and 117.9

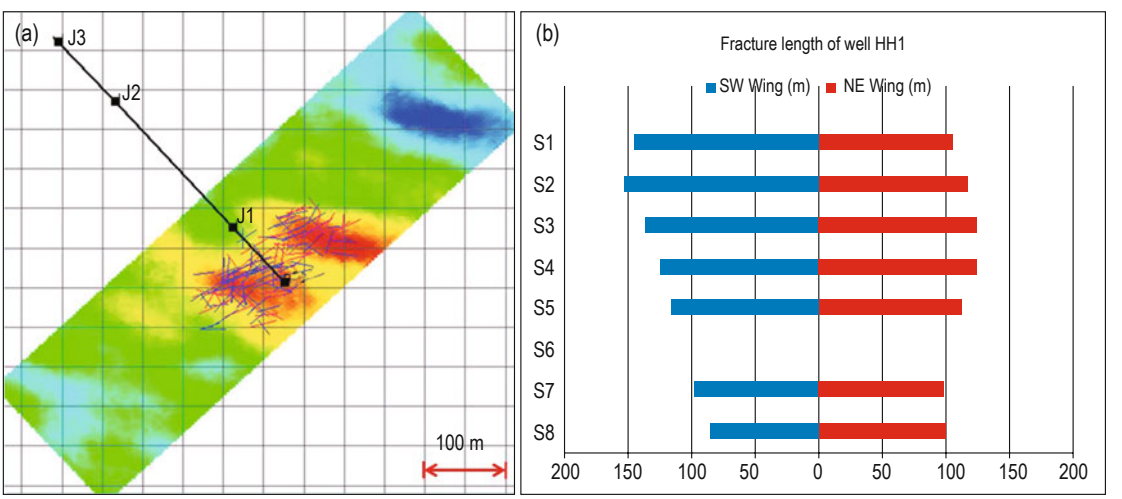

(a) Microseismic monitoring results of the first stage stimulation of well HH1.

(b) Hydraulic fracture length histogram of the eight total stages of well HH1.

Fig.14 The horizontal axis shows hydraulic fracture length and the vertical axis shows stimulation stages where Si represents the ith stage. The red and blue colors represent the length of fractures oriented in the NE and SE directions, respectively.

m. However, the hydraulic fractures have propagated to a longer distance in the SW direction and the hydraulic fracture lengths in the left wing of the fractured zone extend to 145.3 m and 152.9 m. The other stages have not been influenced by the F8 fracture barrier and the fracture lengths of the left and right wings of the wellbore are similar (see Figure 14b).

Conclusions

This case study of the surface-based microseismic monitoring of a six-well group simultaneous stimulation has shown that integration of 3D seismic and microseismic for the characterization of the tight gas reservoir can characterize the reservoir heterogeneity and predict potential fracture barriers before the stimulation, provide the information of the hydraulic fractures during and after the stimulation, and is helpful for adjusting stimulation parameters promptly to avoid any sand plugs. Meanwhile, this study has achieved the following knowledge:

- When the tight gas sand reservoir has strong heterogeneity, the direction of maximum horizontal principle stress conjugates with the direction of minimum horizontal principle stress and the propagation of the hydraulic fractures is controlled by the maximum horizontal principle stress. The propagation direction is identical to the direction of the maximum horizontal principle stress.
- When the orientation of local small faults or fractures is perpendicular to or at wide angles with the direction of local principle stress and the faults or fractures are closed, these faults or fractures can form fracture barriers to prevent the hydraulic fractures from propagating in this direction during the stimulation process.
- When fracture barriers exist on both sides of the wellbore and the hydraulic fractures cannot propagate further on both sides, the hydraulic fracture network will not accept more proppant (sand), in which case sand plugs are prone to occur.

Acknowledgements

In writing this paper, we have received care, support, and help from Professor Peng Su-Ping and Professor Yuan Chun-Fang. In addition, the field acquisition team from the Geophysical Prospecting Company of SINOPEC North China Bureau also provided essential support and help and we express our thanks to all of them.

References

Birkelo, B., Goertz, A., LaBarre, E., et al., 2011, Locating high-productive areas of tight gas-sand reservoirs using LF seismic surveys: 73rd EAGE Conference and Exhibition Incorporating SPE EUROPEC, C016.

Blumentritt, C. H., Marfurt, K. J., and Sullivan, E. C., 2006, Volume-based curvature computations illuminate fracture orientations—Early to Mid-Paleozoic, Central Basin Platform, West Texas: Geophysics, **71**(5), B159 – B166.

Chopra, S., and Marfurt, K. J., 2007a, Curvature attribute applications to 3D surface seismic data: The Leading Edge, **26**(7), 404 – 414.

Chopra, S., and Marfurt, K. J., 2007b, Volumetric curvature attributes for fault/fracture characterization: First Break, **25**(5), 35 – 46.

Chopra, S., and Marfurt, K. J., 2008, Emerging and future trends in seismic attributes: The Leading Edge, **27**(3), 298 – 318.

Chopra, S., and Marfurt, K. J., 2010, Integration of coherence and volumetric curvature images: The Leading Edge, **29**(9), 1092 – 1107.

Duan, C. J., Chen, L. Y., and Wu, H. N., 2009, Development geological characteristics of the Lower Permian overlapping reservoirs in Daniudi Gas Field: Petroleum Geology and Experiment, **31**(5), 495 – 499.

Duncan, M. P., and Eisner, L., 2010, Reservoir characterization using surface microseismic monitoring: Geophysics, **75**(5), 75A139 – 75A146.

Frohne, K.-H., and Mercer, J. C., 1984, Fractured shale gas reservoir performance study- an offset well interference field test: Journal of Petroleum Technology, **36**(2), 291 – 300.

Grechka, V., Mazumdar, P., and Shapiro, S. A., 2010, Predicting permeability and gas production of hydraulic fractured tight sands from microseismic data: Geophysics, **75**(1), B1 – B10.

Hanssen, P., and Bussat, S., 2008, Pitfalls in the analysis of low frequency passive seismic data: First Break, **26**(6), 111 – 119.

Hart, B. S., 2006, Seismic expression of fracture-swarm sweet spots, Upper Cretaceous tight-gas reservoirs, San Juan Basin: AAPG Bulletin, **90**(10), 1519 – 1534.

Kiselevitch, V. L., Nikolaev, A. V., Troitskiy, P. A., et al., 1991, Emission tomography: Main ideas, results, and prospects: 61st Ann. Internat. Mtg., Soc. Expl. Geophys., Expanded Abstracts, 1602 – 1602.

Lakings, J. D., Duncan, P. M., Neale, C., et al., 2006, Surface based microseismic monitoring of a hydraulic fracture well stimulation in the Barnett Shale: 76th Ann. Internat. Mtg., Soc. Expl. Geophys., Expanded Abstracts, 605 – 608.

Lin, C. M., Zhang, X., Zhou, J., et al., 2011, Diagenesis

characteristics of the reservoir sandstones in Lower Shihezi Formation from Daniudi Gas Field, Ordos Basin: Advances in Earth Science, **26**(2), 212 – 223.

Maxwell, S., 2010, Microseismic: Growth born from success: The Leading Edge, **29**(3), 338 – 343.

Maxwell, S., Rutledge, J., Jones, R., et al., 2010, Petroleum reservoir characterization using downhole microseismic monitoring: Geophysics, **75**(5), 75A129 – 75A137.

Maxwell, S., Cho, D., and Nortan, M., 2011, Integration of surface seismic and microseismic Part 2: Understanding hydraulic fracture variability through geomechanical integration: CSEG Recorder, **36**(2), 27 – 30.

Nelson, R., 2001, Geologic analysis of naturally fractured reservoirs: Elsevier, 125 – 162.

Nortan, M., Cho, D., and Maxwell, S., 2011, Integration of surface seismic and microseismic for the characterization of a shale gas reservoir: CSEG Recorder, **36**(1), 31 – 33.

Refunjol, X. E., Marfurt, K. J., and Calvez, J. L., 2011, Inversion and attribute-assisted hydraulically induced microseismic fracture characterization in the North Texas Barnett Shale: The Leading Edge, **30**(3), 292 – 299.

Refunjol, X. E., Marfurt, Keranen, K. M., and Calvez, J. L., et al., 2012, Integration of hydraulic induced microseismic event locations with active seismic attributes: A North Texas Barnett Shale case study: Geophysics, **77**(3), KS1 – KS12.

Ringrose, P., Atbi, M., Mason, D., et al., 2009, Plume development around well KB-502 at the In Salah CO2 storage site: First Break, **27**(1), 85 – 89.

Rutledge, J. T., and Phillips, W. S., 2003, Hydraulic stimulation of natural fractures as revealed by induced microearthquakes, Carthage Cotton Valley gas field, East Texas: Geophysics, **68**(2), 441 – 452.

Shemeta, J., and Anderson, P., 2010, It's a matter of size: Magnitude and moment estimates for microseismic data: The Leading Edge, **29**(3), 296 – 302.

Shen, C., Liang, B. Y., and Li, Z. T., 2009, Principle of vector scanning technique for micro-fractures: Acta Petrolei Sinica, **30**(5), 744 – 748.

Sheriff, R. E. 1991, Encyclopedic dictionary of exploration geophysics, 3rd Edition: SEG Geophysical References Series No.12, 264.

Shi, J., 2009, Application of ant tracking technology in small fault interpretation: Journal of Oil and Gas Technology, **31**(20), 257 – 258.

Song, W. Q., Chen, Z. D., and Mao, Z. H., 2008, Hydro-fracturing break microseismic monitoring technology: China University of Petroleum Press, China, 1 – 3.

Vaidya, V., 2009, Low frequency seismic- A new tool for exploration and development: Drilling and Exploration World, **19**(2), 33 – 37.

Yenugu, M., and Marfurt, K. J., 2011, Relation between seismic curvatures and fractures identified from image logs - application to the Mississipian reservoirs of Oklahoma, USA: 81st Ann. Internat. Mtg., Soc. Expl. Geophys., Expanded Abstracts, 995 – 998.

Zhang, X., 2010, Application of ant tracing algorithm in fault automatic interpretation: a case study on Fangheting structure in Pinghu Oilfield: Oil Geophysical Prospecting, **45**(2), 278 – 281.

Yang Rui-Zhao, PhD, a Senior Engineer in the Research Institute of China New Star Petroleum Company (CNSPC) and now an Associate Professor in the College of Geoscience and Surveying Engineering of the China University of Mining and Technology in Beijing. His research focuses on geological-geophysical comprehensive research on the exploration and development of oil and gas, high-resolution seismic study on CBM and coal field, exploration and development technologies on unconventional resources, and low-permeability reservoir formation restoration, surface based microseismic monitoring of hydraulic fracturing.

APPLIED GEOPHYSICS Vol. 10, No.2 (June 2013)
（应用地球物理）

中文摘要

裂隙张开度对纵波特性与频散影响的实验研究//Effect of crack aperture on P-wave velocity and dispersion, 魏建新[1,2]，狄帮让[1,2]，丁拼博[1,2]，**APPLIED GEOPHYSICS**, 2013, **10**(2), P125-133.
（1. 油气资源与探测国家重点实验室，北京 102249；2. 中国石油大学（北京）CNPC 物探重点实验室，北京 102249）

摘要：为更好地了解裂隙张开度对纵波特征（速度、振幅和各向异性）的频率响应，在实验室利用分层嵌入低速薄圆片模拟裂隙方式，构建了六块裂隙密度为 8.30% 的不同张开度裂隙模型，用四种主频 (0.1 MHz ～ 1MHz) 超声纵波换能器在裂隙模型的平行和垂直裂隙方向上测试了透射纵波速度和振幅。实验数据表明，在 0.1MHz ～ 1MHz 频段范围，张开度从 0.1mm 增大到 0.34mm 时，纵波平行裂隙方向传播时的振幅随频率线性下降，速度频散从 1.5% 增加到 2.1%。垂直裂隙方向传播时振幅随频率呈二次函数缓慢下降，速度频散从 1.9% 到 4.7%。两方向的速度频散差异加剧了张开度模型的各向异性频散。裂隙张开度对纵波特性的频散是由裂隙张开度的散射引起的。
关键词：裂隙张开度，纵波特征，频散，各向异性，实验观测

线源二维时间域瞬变电磁二次场数值模拟//Numerical modeling of the 2D time-domain transient electromagnetic secondary field of the line source of the current excitation, 刘云[1]，王绪本[2]，王赟[1]，**APPLIED GEOPHYSICS**, 2013, **10**(2), P134-144.
（1. 中国科学院地球化学研究所矿床地球化学国家重点实验室，贵阳 550002；2. 成都理工大学地球物理学院，成都 610059）

摘要：本文在 Oristaglio 等（1984）和 Adhidjaja 等（1985）工作基础上，给出线源二维时间域瞬变电磁二次场的 DuFort-Frankel 有限差分数值解，有效避免了在总场求解法中场源附近的奇异问题，并对地 - 空边界电导率的处理、归一化感应电动势偏导数的计算、推进时间步的确定，提出了改进方法；吸取前人成就中二次场地 - 空边界向上延拓和零值边界处理技术，从而简化了计算方法；通过对均匀大地、水平层状大地模型的计算，二次场求解法与解析法的最大相对误差小于 0.01%，计算速度比总场求解法提高了约 3 倍；模拟计算不同时刻瞬变电磁场在地下的分布形态，描绘出感应涡流向下向外的传播特征，以及与地下异常体相互作用的物理过程。
关键词：时间域瞬变电磁，二维，二次场，DuFort-Frankel 有限差分，数值模拟

基于横波射线弹性阻抗的岩性和流体识别研究//Study of S-wave ray elastic impedance for identifying lithology and fluid, 龚雪萍[1,2]，张峰[1,2]，李向阳[1,2]，陈双全[1,2]，**APPLIED GEOPHYSICS**, 2013, **10**(2), P145-156.
（1. 中国石油大学 (北京) “油气资源与探测”国家重点实验室，北京 102249；2. 中国石油大学 (北京)CNPC 物探重点实验室，北京 102249）

摘要：本文推导了关于射线参数的横波（SS）反射系数近似及横波射线弹性阻抗（SREI）表达式。SREI 可以写成 S- 波入射角或者 P- 波反射角的表达式，分别记作 SREIS 和 SREIP。由井资料计算得到的弹性模型表明 SREIP 比 SREIS 及一般的横波弹性阻抗（SEI）具有更强的储层岩性和流体识别能力。Castagna 和 Smith (1994) 收集的 25 种样本表明大角度 SREIP 比一般流体因子具有更好的流体识别能力。每个样本包含一组泥岩、含水砂岩和含气砂岩。实际应用也表明，由纵横波阻抗计算得到的大角度 SREIP 能有效识别致密含气砂岩储层。
关键词：横波，阻抗，射线参数，岩性识别，流体指示

三维地震属性及微地震数据在致密砂岩气藏开发中的综合应用//Integrated application of 3D seismic and microseismic data in the development of tight gas reservoirs, 杨瑞召[1]，赵争光[1]，彭维军[1]，谷育波[1]，王占刚[1]，庄熙勤[2]，**APPLIED GEOPHYSICS**, 2013, **10**(2), P157-169.
（1. 中国矿业大学（北京）地球科学与测绘工程学院，北京 100083；2. 中国石化华北石油局地球物理勘探公司，新乡 453000）

摘要：非常规资源如页岩气和致密砂岩气的开发，要求综合利用多学科的知识，以解决诸多工程问题来获得经济产能。不同类型数据如三维地震和微地震数据所揭示出的储层非均质性能，更深入全面地揭示储层特性并优化钻井和完井程序。本文研究中，首先利用三维地震曲率属性预测了储层局部应力方向及天然裂缝闭合状态，获得了储层非均质性信息及地质力学性质；利用蚂蚁体预测了储层裂缝网络以及利用曲率和蚂蚁体结合预测了潜在的影响水力裂缝延伸的压裂屏障。其次利用三维地震获得的上述信息指导压裂方案设计及施工参数调整。最后，综合三维地震解释结果和微地震成像结果解释了压裂施工过程中出现砂堵的原因，明确了致密砂岩储层水力裂缝延伸及天然裂缝开启闭合控制因素。

关键词：致密砂岩气，三维地震，微地震，油藏描述，水力压裂，压裂屏障

基于压缩感知理论与傅立叶变换的地震数据重建//Seismic data reconstruction based on CS and Fourier theory, 张华[1,2]，陈小宏[1]，吴信民[2]，**APPLIED GEOPHYSICS**, 2013, **10**(2), P170-180.

(1. 东华理工大学放射性地质与勘探技术国防重点学科实验室，江西抚州 344000；2. 海洋石油勘探国家工程实验室，中国石油大学（北京），北京昌平 102249)

摘要：传统的地震勘探数据采样必须遵循奈奎斯特采样定理，而本文基于新发展的压缩感知理论，在突破传统采样定理限制的基础上，利用随机欠采样方法将传统规则欠采样所带来的互相干假频转化成较低幅度的不相干噪声，从而将数据重建问题转为更简单的去噪问题。在数据重建过程中引入凸集投影算法（POCS），采用指数规律衰减的阈值参数，在每次迭代过程中，改变以往从时间到空间都需要进行正反变换的做法，提出只对地震数据空间方向进行正反变换，从而可以减少内存空间，提高运算速度，并且也分析了本文 POCS 算法的抗噪声与反假频能力，同时我们也对二维和三维地震数据重建进行了比较。理论模型和实际数据表明本文方法效果明显，这对于指导复杂地区数据采集、缺失地震道重建及降低勘探成本方面具有重要的实用价值。

关键字：傅立叶变换，压缩感知，凸集投影，数据重建

基于 *L0* 范数最小化的地球物理数据稀疏重构//Geophysical data sparse reconstruction based on *L0*-norm minimization, 陈国新，陈生昌，王汉闯，张博，**APPLIED GEOPHYSICS**, 2013, **10**(2), P181-190.

（浙江大学地球科学系，杭州 310027）

摘要：在实际的地球物理数据采集工作中，会因为多方面的客观原因导致数据缺失，对缺失数据进行插值重构是地球物理数据处理和解释的基础问题。基于地球物理数据自身或在变换域内的稀疏性，将地球物理数据的重构转化为稀疏优化问题可提高数据重构的精确度与稳定性。本文建立了 *L0* 范数最小化的地球物理数据稀疏重构模型，针对不同规模、不同特征的地球物理数据引入了两种不同类型的 *L0* 范数最小优化问题的近似求解算法，即基于 *L0* 范数最小化的迭代再加权最小二乘算法与具有快速收敛性的快速迭代硬阈值法。理论分析与数值试验表明，将迭代再加权最小二乘算法应用到位场数据重构中可发挥其收敛速度快，计算时间短，精度高的优势，而快速迭代硬阈值法更适合处理地震数据，相对于传统的迭代硬阈值法计算效率有了很大的提高。

关键字：地球物理数据，稀疏重构，*L0* 范数最小化，迭代再加权最小二乘，快速迭代硬阈值

稀疏约束反褶积方法实验分析与应用研究//Experimental analysis and application of sparsity constrained deconvolution, 李国发[1]，秦德海[1]，彭更新[2]，岳英[3]，翟桐立[3]，**APPLIED GEOPHYSICS**, 2013, **10**(2), P191-200.

（1. 中国石油大学（北京）油气资源与探测国家重点实验室，北京 102249；2. 中国石油天然气股份公司塔里木油田分公司，库尔勒 841000；3. 中国石油天然气股份公司大港油田分公司，天津 300280 ）

摘要：稀疏条件约束下的反褶积方法突破了地震资料有效频带的限制，能够获得较常规反褶积方法更高的分辨率。但这类反褶积方法存在较强的多解性，且对于弱反射有压制作用。柯西约束、修正柯西约束和 Huber 约束是稀疏反褶积方法常用的约束准则，本文利用模型数据对不同约束准则条件下稀疏约束反褶积恢复反射系数和保护弱反射的能力进行了实验分析。实验结果表明，稀疏约束反褶积的效果取决于约束准则与反射系数概率分布特征的一致程度，修正柯西约束较其它约束准则能够更好地保护弱反射信号。在模型实验的基础上，利用测井数据对碎屑岩地层和碳酸盐岩地层的反射系数概率分布特征进行了统计分析，采用修正柯西约束反褶积方法对实际地震资料进行了实验处理，较大幅度地提高了地震数据分辨率。

关键词：稀疏反褶积，约束准则，修正柯西，分辨率